Vibronic structure of the permanganate absorption spectrum from time-dependent density functional calculations

Neugebauer, J.; Baerends, E.J.; Nooijen, M.A.Th.F.

published in
Journal of Physical Chemistry A
2005

DOI (link to publisher)
10.1021/jp0456990

document version
Publisher's PDF, also known as Version of record

Vibronic Structure of the Permanganate Absorption Spectrum from Time-Dependent Density Functional Calculations

Johannes Neugebauer* and Evert Jan Baerends*

Theoretical Chemistry, Vrije Universiteit Amsterdam, De Boelelaan 1083, 1081 HV Amsterdam, The Netherlands

Marcel Nooijen*

Department of Chemistry, University of Waterloo, 200 University Avenue West, Waterloo, Ontario N2L 3G1, Canada

Received: September 22, 2004; In Final Form: November 23, 2004

The UV absorption spectrum of the permanganate anion is a prototype transition-metal complex spectrum. Despite this being a simple d^0 T_d system, for which a beautiful spectrum with detailed vibrational structure has been available since 1967, the assignment of the second and third bands is still very controversial. The issue can be resolved only by an elucidation of the intricate vibronic structure of the spectrum. We investigate the vibronic coupling by means of linear-response time-dependent density functional calculations. By means of a diabatizing scheme that employs the transition densities obtained in the TDDFT calculations in many geometries around R_e, we construct a Taylor series expansion in the normal coordinates of a diabatic potential energy matrix, coupling 24 excited states. The simulated vibronic structure is in good agreement with the experimental absorption spectrum after the adjustment of some of the calculated vertical excitation energies. The peculiar blurred vibronic structure of the second band, which is a very distinctive feature of the experimental spectrum, is fully reproduced in the calculations. It is caused by the double-well shape of the adiabatic energy surface along the Jahn−Teller active e mode of the allowed ^1E state arising from the second $^1T_2$ state, which exhibits a Jahn−Teller splitting into $^1B_2$ and ^1E states. We trace the double-well shape to an avoided crossing between two diabatic states with different orbital-excitation character. The crossing can be explained at the molecular orbital level from the Jahn−Teller splitting of the set of $7t_2\{3d_{xy}, 3d_{xz}, 3d_{yz}\}$ orbitals (the LUMO + 1), to which the excitations characterizing the diabatic states take place. In contrast to its character in the two well regions, at R_e the 2^1T_2 state is not predominantly an excitation to the LUMO + 1, but has more HOMO − 1 → LUMO ($2e = \{3d_{x^2-y^2}, 3d_{z^2}\}$) character. The changing character of the $2^1T_2 - {}^1E$ state along the e mode implies that the assignment of the experimental bands to single orbital transitions is too simplistic intrinsically. This spectrum, and notably the blurring of the vibronic structure in the second band, can be understood only from the extensive configurational mixing and vibronic coupling between the excited states. This solves the long-standing assignment problem of these bands.

1. Introduction

The UV absorption spectrum of the tetrahedral d^0 complex MnO_4^- has become a prototype spectrum in transition-metal spectroscopy. A well-resolved experimental spectrum was published in 1967 by Holt and Ballhausen.[1] Four band systems can be seen in this spectrum: (i) a very strong band with an origin at ca. 18 000 cm^{-1} with a very distinct strong vibrational progression of 770 cm^{-1}, (ii) a somewhat weaker band between 25 000 and 30 000 cm^{-1}, starting with two low-intensity peaks at ca. 25 000 and 25 700 cm^{-1} followed by the main part in which the vibrational structure is remarkably blurred, which is superimposed with (iii) a strong band starting at 30 000 cm^{-1} with distinct, regular vibrational spacing of 750 cm^{-1}, and (iv) an intense, completely featureless band with its origin at 38 500 cm^{-1}. An early review of the electronic absorption spectrum of MnO_4^- can be found in ref 2.

The permanganate ion is one of the benchmark systems for the assessment of excitation energies from quantum chemical methods, and many calculations of excitation energies have been performed for this system. It is not easy to deduce vertical transition energies from the experimental bands, and the intricate vibronic structure of the spectrum as well as the expected Jahn−Teller splittings of the allowed excited $^1T_2$ states indicate the necessity of a vibronic coupling treatment for a meaningful comparison of the theory and experiment. This has been lacking until now. The discussion has been mostly in terms of an assignment of the experimental bands to single orbital transitions, on which there is still disagreement between the various quantum chemical methods. The energetic order of the orbitals near the HOMO−LUMO gap is shown in Figure 1. In this d^0 system, the LUMO and LUMO + 1 are the d orbitals, 2e and $7t_2$ exhibiting the ligand field splitting through antibonding mixing with the oxygen 2p, and the highest occupied levels are the 12 fully occupied oxygen 2p lone pair orbitals. The highest of these are the HOMO $1t_1$, which is 100% 2p by symmetry, and the HOMO − 1 $6t_2$, which has very little d admixture. Below these nonbonding levels are the $6a_1$, which is somewhat stabilized by admixture of the 4s, and the 1e and $5t_2$ levels,

* E-mail: jneugeb@chem.vu.nl, baerends@chem.vu.nl, nooijen@uwaterloo.ca.

10.1021/jp0456990 CCC: $30.25
Published on Web 01/21/2005

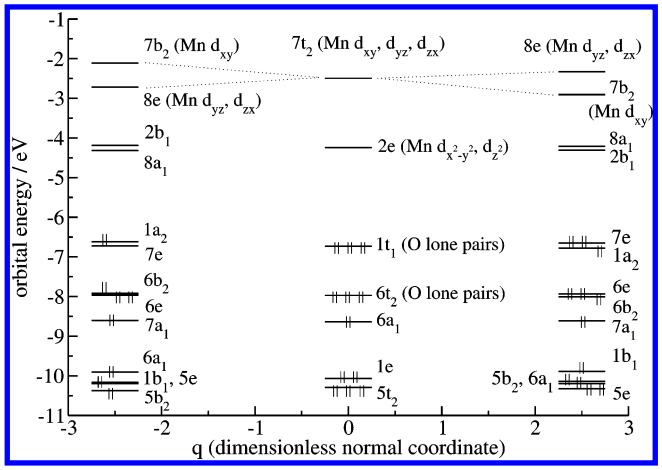

Figure 1. Energetic ordering of the molecular orbitals of MnO_4^- near the HOMO−LUMO gap from SAOP/TZ2P calculations. The orbital energies are shown for the ground-state equilibrium structure and structures displaced along the Q_θ mode by $\Delta q = \pm 2.5$.

which represent 2p orbitals that are more strongly stabilized by admixture with the 3d.

Despite much theoretical effort, see below, the assignment of the experimental bands to specific orbital transitions is by no means established. With the exception of early extended Hückel, Hartree−Fock (HF), and CI-singles calculations, which proved to be rather unreliable, all of the theoretical methods agree with the assignment of the first band, which is of the HOMO → LUMO ($1t_1 \rightarrow 2e$) type. The fourth band is mostly attributed to a HOMO − 1 → LUMO + 1 ($6t_2 \rightarrow 7t_2$) transition (with another strong contribution from the $6a_1 \rightarrow 7t_2$ transition, which is actually dominant in SAC-CI[3] calculations). There is, however, still a strong controversy about the assignment of the second band to either the $6t_2 \rightarrow 2e$ or $1t_1 \rightarrow 7t_2$ transition (and the third band, then, to the other transition). It is a typical case of doubt whether the HOMO − 1 → LUMO or the HOMO → LUMO + 1 transition is lowest in energy. The issue remains unresolved, although this particular electronic absorption spectrum has been a real testbed for electronic structure methods. Wolfsberg and Helmholtz[4] pioneered the extended Hückel method in 1952 with an MO study of this spectrum, followed by several other such studies (e.g., refs 5 and 6). The multiple-scattering Xα method, despite its muffin-tin approximation, made its mark on transition-metal chemistry in 1971 with a remarkably successful calculation[7] of the permanganate spectrum using Slater's transition-state method. This calculation assigned the second band to the HOMO − 1 → LUMO (i.e., $6t_2 \rightarrow 2e$) transition. This is actually in disagreement with the assignment advocated in the experimental study by Holt and Ballhausen[1] in which it was the third band that was assigned to the HOMO − 1 → LUMO transition. Shortly afterward, after a basis function Xα method that avoided the muffin-tin approximation had been developed,[8] one of the first applications of this method in 1976 was to an extensive series of tetrahedral oxoanions including permanganate.[9] These latter calculations partly resolved multiplet states with the diagonal sum method. The assignment agreed with the MSXα assignment. Much later, in 1996, a similar "ΔSCF" DFT (GGA) calculation, which used the calculation of a few selected two-electron integrals to obtain full resolution of the multiplet states, reversed the assignment.[10] However, a subsequent LDA (local density approximation) calculation of a similar type in 1997[11] did not lead to the reversed assignment and neither did other such DFT calculations with either the ΔSCF method[12] or the practically equivalent transition-state method.[13] There are two published time-dependent DFT calculations (1999[14] and 2001[15]) that have both sided with the original Xα assignment, but because the errors in the vertical excitation energies from many of the DFT calculations are larger than the splitting between these two states, no reliable assignment can be made on their basis. Also, the ab initio calculations do not offer a clear picture. Skipping HF (ΔSCF)[16,17] and CIS[16] calculations in the early 1970s, which proved to be unreliable, we note that the CISD calculations of Johansen and Rettrup in 1983[18] assign the $6t_2 \rightarrow 2e$ to the second band, in agreement with the Xα calculations. SAC-CI calculations[3] reversed the assignment in 1991, (ST)EOM-CCSD[19] went back to the original assignment in 1999, but extended STEOM-CC calculations[20] reversed it again in 2000.

The experimental energy difference of about 0.3 eV for the second and third transitions is of the same order of magnitude as the error in the TDDFT calculations and is about the order of magnitude of possible errors in any theoretical method to date for a transition-metal complex. As indicated earlier, a vibronic coupling treatment is required for a full elucidation of the intricate vibrational structure of the spectrum and to settle the assignment problem. Because the second band has such a different vibrational structure compared to that of the third (and first) band, one could place some confidence in an assignment based on a vibronic coupling treatment if the latter would be able to reproduce and explain this feature. One method of studying the vibronic structure of electronic absorption spectra is the Franck−Condon approach. It has recently been applied successfully in combination with TDDFT excited-state optimizations to model the absorption spectra of organic compounds by Dierksen and Grimme.[21,22] As has been mentioned in ref 23, however, the Franck−Condon approach might have problems in some cases if (i) the excited-state minimum is largely displaced from the ground-state minimum, (ii) there are (near-) degenerate excited states that result in a complicated topology of the potential energy surfaces (PESs), or (iii) no excited-state minimum due to, for example, conical intersections can be found.

An alternative treatment,[23] which is used in this work, is based on the short-time approximation for absorption and resonance Raman scattering (see, for example, refs 24−29). It uses a Taylor series expansion around the ground-state equilibrium of quasi-diabatic excited-state surfaces and coupling matrix elements between them, so nonadiabatic couplings between excited states are also taken into account.

In this article, we show that the general vibronic features of the absorption spectrum of permanganate can be reproduced within this vibronic coupling scheme, including the vibrational structure due to Jahn−Teller active normal modes that lead to minima at distorted (lower-symmetry) geometries. Our spectra simulations demonstrate that the energy surfaces obtained with the asymptotically correct SAOP potential (statistical averaging of (model) orbital potentials),[30−32] which we employ in our calculations, lead to a vibronic structure in agreement with the experimental findings, although the accuracy of the vertical transition energies is, with errors of up to 0.9 eV, poorer than usual. Although we can resolve the controversy over the orbital assignments for the excited states at R_e on this basis, the more important conclusion is that a single-orbital transition picture is much too simple to explain the complicated structure of the absorption spectrum of permanganate.

TABLE 1: Excitation Energies (E_{ex} in eV) and Oscillator Strengths (f)[a] of the Excited States of Irreducible Representation T_2 of the Permanganate Ion Calculated from SAOP with Different Basis Sets[b]

					SAOP						
						TZ2P		QZ3P		QZ3P-3DIF	
no.	transition	exptl[1]	EOM-CCSD[19]	Ext-STEOM[20]	TZ2P/COSMO[37]	E_{exptl}	f	E_{exptl}	f	E_{exptl}	f
1	$1t_1 \rightarrow 2e$	2.3	2.24	1.92	2.87	3.01	0.0070	2.98	0.0070	2.98	0.0073
2	$6t_2 \rightarrow 2e$	3.5	3.60	3.51	3.89	4.04	0.0021	4.02	0.0023	4.01	0.0024
3	$1t_1 \rightarrow 7t_2$	4.0	3.67	3.08	4.77	4.93	0.0086	4.88	0.0100	4.87	0.0104
4	$6t_2 \rightarrow 7t_2$	5.5	5.80		5.77	5.95	0.0023	5.92	0.0028	5.91	0.0035

[a] Not multiplied by degeneracy. [b] All of the values are calculated at the BPW91/TZ2P optimized geometry (Mn−O distance: 1.621 Å). The experimental values shown are the positions of the band maxima of the spectrum reported in ref 1. The SAOP/TZ2P/COSMO,[37] EOM-CCSD,[19] and extended-STEOM-CC[20] values are given for comparison.

2. Methodology

Density functional calculations have been performed using a modified version of the Amsterdam density functional (ADF) package.[33,34] We used the SAOP potential[30−32] in combination with the TZ2P, the even-tempered QZ3P, and the QZ3P-3DIFFUSE (including three sets of diffuse functions) basis sets from the ADF basis set library[33] to calculate TDDFT transition densities and vertical excitation energies for structures displaced from the ground-state equilibrium along the normal coordinates. The construction of diabatic states and effective Hamiltonians follows the approach in refs 23 and 35.

The effective Hamiltonian consists of the kinetic energy operator for the nuclei and a potential energy matrix in the diabatic basis. For the latter, we use a Taylor series expansion around the equilibrium structure

$$\mathbf{V}(\mathbf{q}) = \mathbf{V}(\mathbf{0}) + \sum_{i=1}^{N_q}\left(\frac{\partial \mathbf{V}}{\partial q_i}\right)_0 q_i + \frac{1}{2}\sum_{i,j=1}^{N_q}\left(\frac{\partial^2 \mathbf{V}}{\partial q_i \partial q_j}\right)_0 q_i q_j + \cdots \qquad (1)$$

where q_i are the normal coordinates of the system. The matrix elements V_{ab} of the $\mathbf{V}$ matrix are between diabatic electronic states, which are constructed to have an (almost) constant electronic part along the normal modes (see below). We distinguish between the intrastate matrix elements V_{aa}, intramultiplet matrix elements V_{ab}, where a and b refer to states belonging to the same multiplet, say n^1T_2, and intermultiplet matrix elements V_{ab}, where a and b belong to different multiplets (e.g., n^1T_2 and m^1T_2). If we ignore the off-diagonal matrix elements, the intrastate linear Taylor expansion terms $(\partial V_{aa}/\partial q_i)_0$ (still called coupling constants) would account for the displacement of the minimum with respect to $q_i = 0$ and the diagonal (in the normal coordinates) quadratic coupling constants $(\partial^2 V_{aa}/\partial q_i^2)_0$ would account for the changes in vibrational frequency in the excited states. (The default value for a diagonal intrastate quadratic coupling constant is just the ground state $\omega_{0,i}$.) We include all of the linear coupling constants and the diagonal quadratic coupling constants in principle for all of the matrix elements of $\mathbf{V}$ (both intrastate and interstate).

The derivatives of the potential energy matrix elements with respect to the normal coordinates are calculated by numerical differentiation of the diabatic potential energy matrix elements, the latter being explicitly calculated at displaced structures, $V_{ab}(\pm\Delta q_i)$. A diabatic matrix at a particular Δq_i is constructed by a unitary transformation of the diagonal adiabatic potential energy matrix containing the vertical excitation energies for that particular structure

$$\mathbf{V}(\mathbf{q}) = \mathbf{U}^{\dagger}(\mathbf{q})\,\mathbf{E}^{\mathrm{elec}}(\mathbf{q})\,\mathbf{U}(\mathbf{q}) \qquad (2)$$

The vertical excitation energies, which constitute the diagonal matrix $\mathbf{E}^{\mathrm{elec}}(\mathbf{q})$, are obtained from the TDDFT calculation. The transformation matrices $\mathbf{U}(\mathbf{q})$ are calculated in such a way that the overlap matrix of transition densities is maximally diagonal in the diabatic basis. For details, we refer to the description of the algorithm in ref 35 and the related approach in ref 23. The vibronic coupling simulations based on the diabatic potential energy matrix are carried out using the VIBRON program package.[36] We included up to 24 excited states and up to 1 474 560 vibrational basis functions for each state (in the full simulation). The total dimension of the vibronic problem (i.e., of the model Hamiltonian to be diagonalized) is therefore 35 389 440. Despite this large dimension, such simulations are fairly routine because an interface between ADF and VIBRON allows a user-friendly combination of electronic structure and vibronic coupling calculations. The computational cost, however, increases rapidly with the number of quanta in the individual modes and the number of excited states included in the simulation.

3. Vertical Excitations

We calculated the vertical excitation energies for the $^1T_2$ excitations of MnO_4^- with the TZ2P basis, which is also used to model the vibronic structure. The results are compared to those obtained with the larger QZ3P and QZ3P-3DIFFUSE basis sets; in the latter calculations, three additional sets of diffuse functions are used for the oxygen atoms, whereas we employed the QZ3P basis set for the central manganese atom. From the vertical excitation energies for the permanganate anion listed in Table 1, it can be seen that the TZ2P basis set already leads to results that are almost converged. The excitation energies change by less than 0.1 eV when increasing the basis set.

Although the above results were obtained with the structure optimized with BPW91/TZ2P (Mn−O distance: 1.621 Å), we also calculated excitation energies for the structures optimized with the larger basis sets. But structural changes or changes in the excitation energies can hardly be recognized. (The Mn−O distance for both BPW91/QZ3P and BPW91/QZ3P-3DIFFUSE is 1.620 Å.)

For some transitions, the vertical excitation energies differ considerably from those of the experiment (i.e., by between 0.5 and 0.9 eV). The SAOP results in ref 37, which included environmental effects in the form of the COSMO solvation model and are given in Table 1 for comparison, demonstrate that environmental effects can lead to a lowering of the excitation energies, but these effects are certainly not large enough to explain such large discrepancies between the experiment and the calculation. Furthermore, the solvation model leads mainly to an overall shift in the excitation energies (i.e., incorrect *energy gaps* between different excited states are hardly corrected). Deficiencies in the SAOP potential or the exchange-correlation kernel or both are thus most likely responsible for this disagreement. We will concentrate on the vibrational

TABLE 2: Orbital Contributions (in %) for the Excited States in Irreducible Representation E of the Permanganate Ion along the Q_θ Mode Calculated from SAOP/TZ2P[a]

	orange curve ("2^1T_1")					lower green curve ("2^1T_2")					("3^1T_1")				
	4E	3E	($2T_1$)	3E	4E	3E	4E	($2T_2$)	4E	3E	5E		($3T_1$)	5E	
Δq	−6	−2.5	0	2.5	6	−6	−2.5	0	2.5	6	−6	−2.5	0	2.5	6
($1t_1 \rightarrow 2e$)															
$7e \rightarrow 8a_1$	2									9	1	1		3	3
$7e \rightarrow 2b_1$						3					2	2			
($6t_2 \rightarrow 2e$)			(96)					(68)					(2)		
$6e \rightarrow 8a_1$	75	72	72	76	75	10	17	17	2	3	7	2	2	17	20
$6e \rightarrow 2b_1$	19	25	24	2	22	9	29	51	58	13	62	30		16	45
($1t_1 \rightarrow 7t_2$)			(4)					(30)					(96)		
$1a_2 \rightarrow 8e$	2	2	2		2	77	53	15	2		8	32	48	31	13
$7e \rightarrow 7b_2$	1	1	2	20				15	37	73	7	26	48	28	6
($6t_2 \rightarrow 7t_2$)															
$6e \rightarrow 7b_2$										1				4	12
$6b_2 \rightarrow 8e$											10	4			
(others)															
$7a_1 \rightarrow 8e$	14						16		1		3	1			

	upper green curve ("3^1T_2")					("4^1T_1")				
	7E	6E	($3T_2$)	6E	7E	6E	7E	($4T_1$)	7E	6E
Δq	−6	−2.5	0	2.5	6	−6	−2.5	0	2.5	6
($1t_1 \rightarrow 2e$)			(3)							
$7e \rightarrow 8a_1$		1	3	1	2				1	
$7e \rightarrow 2b_1$										
($6t_2 \rightarrow 2e$)			(16)							
$6e \rightarrow 8a_1$	1	3	4	1					1	
$6e \rightarrow 2b_1$	1	5	12	9	10		2		2	
($1t_1 \rightarrow 7t_2$)			(56)							
$1a_2 \rightarrow 8e$		5	28	57	49		1		3	30
$7e \rightarrow 7b_2$	69	64	28	5	3	13	2		2	
($6t_2 \rightarrow 7t_2$)			(20)					(98)		
$6e \rightarrow 7b_2$	1	3	10	21	13		10	49	61	68
$6b_2 \rightarrow 8e$	1	15	10	4	12	71	66	49	22	
(others)										
$7a_1 \rightarrow 8e$	24	3	3		5		16		5	

[a] For the ground-state equilibrium structure ($\Delta q = 0$), these states belong to either the T_1 (for n^1E states with n as an odd number) or the T_2 irreducible representation (for n^1E states with n as an even number). The values and labels corresponding to the T_d structures are given in parentheses; all other labels and entries in the table refer to D_{2d} symmetry. Note that where possible we follow the auxiliary (colored) curves in Figure 5 instead of pure adiabatic potential energy curves.

structure of the absorption bands in this study, which depend on the shapes of the potential energy surfaces and not directly on their vertical positions.

Table 1 also shows the dominant orbital transitions for the given excitations. The assignment given here is in agreement with previous studies using TDDFT.[14,15] Consequently, it agrees with the original DFT calculation of ref 9 and the more recent DFT calculations from refs 11 and 12, which are all of the ΔSCF type (sometimes approximated with Slater's transition-state procedure), but it differs from some calculations (e.g., from the DFT-ΔSCF calculation in ref 10) and reverses the orbital assignments for these states. However, we will argue (see below) that these assignments in terms of orbital transitions are not meaningful. From the contributions of the orbital transitions to the different excited states, which are listed in Table 2 and will be discussed in the next section, it can be seen that for all excited states besides 1^1T_2 important mixings of singly excited configurations occur, so an assignment of the absorption spectrum in terms of single orbital transitions is apparently inadequate.

4. Potential Energy Curves

4.1. Assessment of the Model Potential Curves. In the upper panel of Figure 2, we show the calculated adiabatic energy points for the excited states of $^1T_2$ symmetry along the totally symmetric Mn−O stretching mode, which is the most important mode for the vibrational structure. In this panel, we also give the model PESs that were obtained by diagonalization of the $\mathbf{V}(\mathbf{q})$ matrix for these $^1T_2$ states using the Taylor expansion with linear and quadratic coupling constants $(\partial V_{ab}/\partial q_1)_0$ and $(\partial^2 V_{ab}/\partial q_1^2)_0$, with q_1 being the a_1 mode for all of the intrastate and interstate matrix elements. The curves are obtained by calculating the $\mathbf{V}$ matrix from the Taylor expansion and diagonalizing it in a dense set of q_1 values, keeping all other q_i equal to zero.

The model curves are in very good agreement with the explicitly calculated points near the equilibrium position. There is very little coupling between the different electronic states along this mode. We expect vibrational states that can be clearly associated with the individual electronic states, and because all curves exhibit a minimum that is somewhat displaced toward a longer Mn−O bond length, we expect a typical Franck−Condon intensity pattern of the vibrational states (with vibrational spacing of approximately 800 $cm^{-1} \approx 0.1$ eV, the second peak will be most intense). The a_1 vibrational structure will dominate the spectrum because of the large displacements of the excited-state minima from the ground-state equilibrium position.

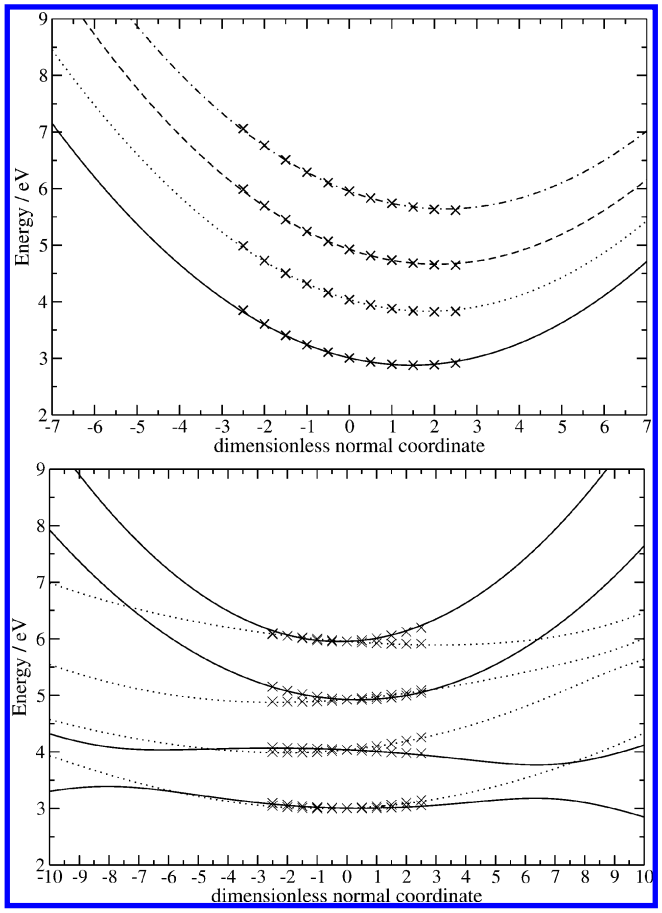

Figure 2. Adiabatic model potential energy curves for the lowest $^1T_2$ excited states along the modes of a_1 (top) and e (bottom) symmetry (the Q_θ component, see Figure 3). The latter mode is Jahn−Teller active and leads to a splitting of the degenerate states into a doubly degenerate ^1E (solid lines) and a $^1B_2$ state (dotted lines). Also shown are the data points for explicitly calculated excited-state energies for structures displaced along these normal coordinates.

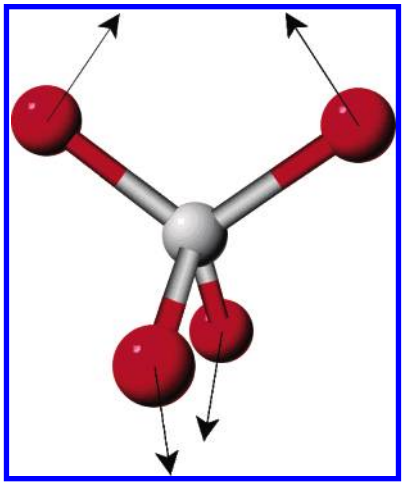

Figure 3. Normal mode of e symmetry for MnO_4^-, for which the potential energy surface in Figure 2 is shown (Q_θ).

In the lower panel of Figure 2, we show the calculated points and adiabatic model curves for the Jahn−Teller active mode of e symmetry. For this comparison, we chose the mode depicted in Figure 3 from the set of two degenerate modes. It corresponds to the $Q_\theta(X_1 - X_2 - X_3 + X_4)$ symmetrized displacement according to ref 38 and leads to a D_{2d} symmetric structure, in which two of the three former degenerate $^1T_2$ states fall into irreducible representation E and remain degenerate (solid curves), whereas the third one is of B_2 symmetry (dotted curves). The model curves follow the calculated points perfectly close to the equilibrium geometry, so the second-order Taylor expansion is adequate.

The system investigated here is much more complicated than the prototype T−e Jahn−Teller system described in ref 39, which can be described by three equivalent paraboloids. Our model PESs are more general (and more complicated) because quadratic couplings are also taken into account and the different sets of triply degenerate states ($^1T_2$ multiplets) can interact, which is, as we will see below, quite essential. Also, the inclusion of diagonal quadratic coupling constants is very important because the curvatures of the PES curves at the $Q_\theta = 0$ point (i.e., at R_e) exhibit large deviations from the curvature of the ground state. For the 2^1T_2 state (^1E for $Q_\theta \neq 0$), it is even negative at $Q_\theta = 0$. This negative curvature of the 2^1T_2 state and the double-minimum shape of this potential energy curve will play an important role in the analysis of the vibronic structure.

The model curves plotted in Figure 2 are obtained from a model including only the $^1T_2$ states, but the states of $^1T_1$ symmetry also have to be considered. Along the Q_θ displacement, all of these states lead to ^1E states in D_{2d} symmetry in addition to a nondegenerate state. Electric dipole transitions from the ground state to the $^1T_1$ states are forbidden in tetrahedral geometry but not to the ^1E states resulting for finite Q_θ, although the intensities would still be very low if the electronic structure is basically unaltered from the one at R_e. However, these ^1E states arising from the $^1T_1$ states can interact (or even exhibit avoided crossings) with the ^1E states coming from the $^1T_2$ states. We therefore included the $^1T_1$ states in our model; the resulting model adiabatic potential energy curves (obtained by diagonalization of the Taylor expanded $\mathbf{V}(\mathbf{Q}_\theta)$ matrix at many Q_θ points) are shown in Figure 4 and are compared to explicitly calculated data points, which are extended along the Q_θ mode to map out the full range of this displacement coordinate that is relevant for the vibrational motions. Our model works quite well close to the reference point, whereas somewhat larger deviations occur, as expected, for a second-order Taylor series at larger displacements. However, all of the qualitative features, such as minima or avoided crossings, are well represented by the model curves. The main discrepancy between the model and the real adiabatic curves is that the latter are much steeper for large displacements in the plus direction (i.e., the direction indicated by the arrows in Figure 3), whereas the agreement in the minus direction is better. Another difference is that the explicitly calculated curve of the 4^1T_2 state is affected by couplings to even higher excited states, which are not included in the vibronic model, so that features arising from these couplings cannot be represented.

4.2. Explanation of Couplings in Terms of Orbital Contributions. To discuss the shape of the adiabatic curves and the electronic structure explanation of these shapes, we first show in Figure 5 the full set of adiabatic potential energy curves arising from the $1-4^1T_2$ states at R_e (solid lines) and from the $1-4^1T_1$ states (dashed lines). These lines simply connect the adiabatic points (i.e., the nth line connects the nth excited-state energies in the diagram ($n = 1-8$)). Note that significant changes may occur in the electronic structure along a particular solid or dashed line because of the occurrence of avoided crossings. For clarity, we introduce some auxiliary states indicated by colored curves in this Figure. As an aid in the interpretation of the states that are crucial for the vibronic structure of the second band in the absorption spectrum, we

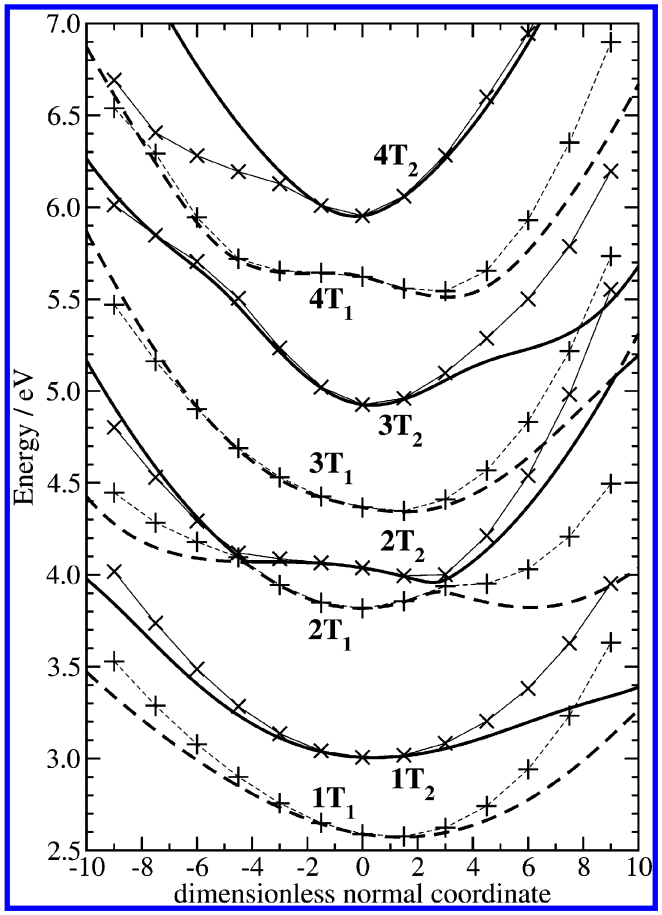

Figure 4. Adiabatic model potential energy curves for the lowest $^1T_1$ and $^1T_2$ excited states along a mode of e symmetry (the Q_θ component, see Figure 3). Only the components of symmetry E for distorted structures are shown. The solid lines indicate the states which are of $^1T_2$ character at the reference structure, whereas the dashed lines are used for those of $^1T_1$ character at R_e. Also shown are the data points for explicitly calculated excited-state energies for structures displaced along these normal coordinates, where we used + signs for the states corresponding to $^1T_1$ and crosses for the states corresponding to $^1T_2$ at the ground-state equilibrium structure. These have been connected with light dashed and solid lines, respectively.

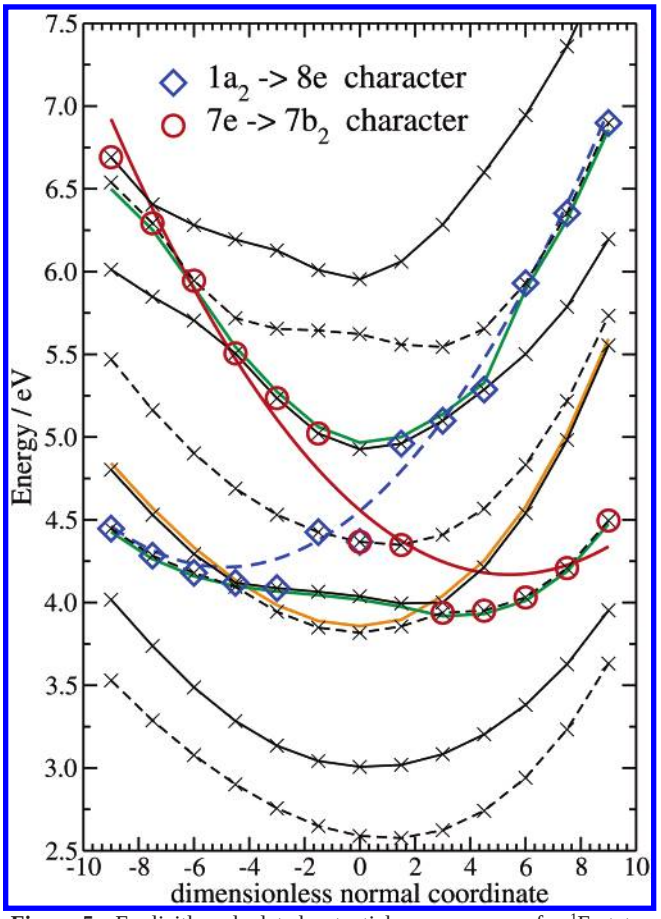

Figure 5. Explicitly calculated potential energy curves for ^1E states of the permanganate anion along the Q_θ mode. Thin (black) dashed lines: ^1E states corresponding to $^1T_1$ states at the equilibrium geometry; thin (black) solid lines: ^1E states corresponding to $^1T_2$ states at the equilibrium geometry. For every displacement, a blue diamond labels the states with the largest contribution of the $1a_2 \rightarrow 8e$ orbital transition, whereas a red circle labels the state with the largest contribution of the $7e \rightarrow 7b_2$ orbital transition for the D_{2d} symmetric, displaced structures. The thick blue dashed and red solid lines are quadratic fits to the data points marked with diamonds and circles, respectively (shifted by 0.05 eV for clarity of presentation).

draw two hypothetical diabatic curves (red and blue) in Figure 5, each of which represents a particular excited-state electronic structure and may be considered to be the parent curves from which the two green ones arise after coupling between these diabatic states has been taken into account. The lower green state, which can be described as the $3^1E-4^1E-2^1T_2-4^1E-3^1E$ energy curve (going from negative to positive Q_θ), will be denoted as "2^1T_2" in the following text.

An avoided crossing that is readily apparent from the Figure is the one at $Q_\theta \approx 2.1$ between the $2^1T_1-3^1E$ (second dashed curve) and "2^1T_2"-4^1E states (second solid curve); it can be understood from a coupling of the orange state ("2^1T_1") and the lower green state. The state indicated in orange has predominant $6e \rightarrow 8a_1$ character throughout the displayed Q_θ range (6e originates from the HOMO − 1 $6t_2$, $8a_1$ originates from the LUMO 2e). At R_e, it corresponds to the electric-dipole-forbidden 2^1T_1, so its vibronic states will have very low intensity, if any. The electronic structure of the allowed state indicated by the lower green curve ("2^1T_2") is less straightforward; it changes considerably along the Q_θ coordinate, which can be explained in terms of the blue and red hypothetical diabatic curves.

The construction of these two hypothetical diabatic states can be understood from and justified with Table 2, where we document the composition of the states at the equilibrium geometry $Q_\theta = 0$ and at four displaced geometries $Q_\theta = \pm 2.5$ and ± 6. The isolated 1^1T_2, which has HOMO $\rightarrow$ LUMO character and is responsible for the first band, needs no further discussion. Although the 2^1T_2 state is clearly dominated by the $6t_2 \rightarrow 2e$ transition (68% at ground-state equilibrium), there is significant mixing with the $1t_1 \rightarrow 7t_2$ configuration (30%). When we follow the curve along first the 4^1E state and after crossing with the ^1E state arising from 2^1T_1 along the 3^1E (i.e., along the green curve in both the positive and negative Q_θ directions), we note that the composition becomes predominantly $1t_1 \rightarrow 7t_2$ (i.e., $7e \rightarrow 7b_2$ at positive Q_θ and $1a_2 \rightarrow 8e$ at negative Q_θ; see Figure 1). In fact, this electronic-structure feature is very important for an understanding of the double-well nature of the "2^1T_2" state (lower green curve). We note that this potential energy curve resembles the model curve of the ^1E state arising from 2^1T_2 in the lower panel of Figure 2, which also has a double minimum. In fact, this state is only slightly perturbed by the avoided crossing with the ^1E state arising from the 2^1T_1 (i.e., by a coupling with the orange curve), which was not included in the lower panel of Figure 2.

Because of the lack of coupling between the orange "2^1T_1" state with the green "2^1T_2" state, the negative curvature of the latter at R_e and its double-well structure will determine the

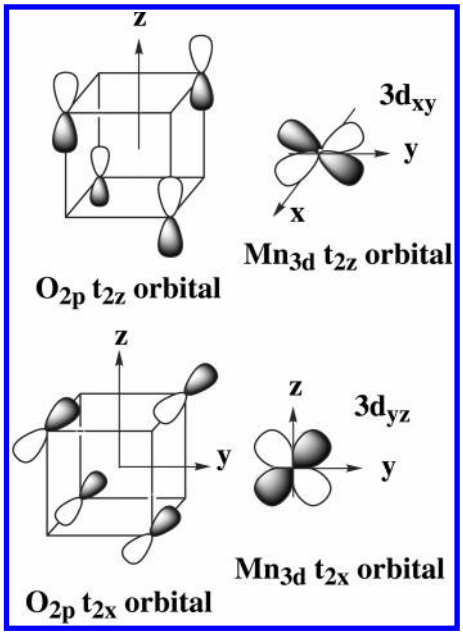

Figure 6. Antibonding interaction of the Mn 3d orbitals of t_2 symmetry ($3d_{xy}$, $3d_{xz}$, $3d_{yz}$) with linear combinations of oxygen 2p orbitals with the same t_2 symmetry.

vibronic structure in this region of the spectrum (the second band). This particular shape of the potential energy curve ultimately explains the blurring of the vibrational structure of the second band in the experiment; see the next section. We therefore first address the nature and cause of the changes in orbital structure of this excited state along Q_θ. The crucial point is the Jahn−Teller splitting of the degenerate orbitals, notably ligand-field level $7t_2$. In Figure 1, we show the orbital energies for the orbitals near the HOMO−LUMO gap for the equilibrium structure and for structures displaced along Q_θ. For most of the orbitals, the splitting of the degenerate sets is very small (i.e., on the order of 0.1 eV). The only exception is the $7t_2$ level, which consists of an antibonding linear combination of the manganese d_{xy}, d_{yz}, and d_{xz} orbitals and the oxygen lone pairs; see Figure 6.

A displacement in the positive direction of the normal mode Q_θ moves the oxygen atoms closer to the z axis so that the antibonding interaction with the orbital with d_{xy} character is decreased and the orbital is stabilized. The d_{yz} and d_{xz} orbitals (8e) are destabilized because their antibonding interaction with the oxygen lone pairs is increased. This change, although certainly nonnegligible (see Figure 1), is weaker than the change for the d_{xy} orbital ($7b_2$), which can be understood from the weaker change along the Q_θ mode in the overlap with the oxygen atoms. For a negative displacement, the effect is exactly the other way around, and again the effect (destabilization in this case) on the $7b_2$ (d_{xy}) orbital is roughly twice as large as the effect (stabilization now) on the 8e (d_{yz}, d_{xz}) orbitals.

The $7e \rightarrow 7b_2$ orbital transition dominates the 3^1E state at a large positive Q_θ. If we had chosen a reference point somewhere between $Q_\theta = 6$ and 9, then our diabatizing scheme would have resulted in a diabatic state with a potential energy curve indicated qualitatively with the red curve in Figure 5, which follows the adiabatic states with the largest $7e \rightarrow 7b_2$ orbital transition contribution (marked with red circles). This (hypothetical) curve is drawn in the Figure just to guide the eye. (N.B. This hypothetical diabatic state is completely different from the diabatic model states that are actually employed in the vibronic coupling simulations. One can make different choices for the diabatic states and couplings between them, and in the calculations, we use diabatic states that have the electronic structure of the adiabatic states at R_e. This choice is purely a matter of computational convenience.) One can read the contribution of the $7e \rightarrow 7b_2$ excitation to the various adiabatic states along the red curve from Table 2. It goes from 73% in 3^1E at $Q_\theta = 6$ to a spread over the $3-5^1E$ states (20, 37, and 28%, respectively) at $Q_\theta = 2.5$, next to 15, 48, and 28% over 4, 5, 6^1E ($= 2^1T_2$, 3^1T_1, 3^1T_2) at $Q_\theta = 0$ and then up to higher ^1E states at negative Q_θ (69% in 7^1E at $Q_\theta = -6$). The energy of the 8e orbitals (d_{xz} and d_{yz}) goes in the opposite direction to that of $7b_2(d_{xy})$, and we have indicated the hypothetical diabatic state corresponding to the $1a_2 \rightarrow 8e$ excitation as a blue curve in the Figure. It is apparent from the Figure that the double-well potential energy curve corresponding to the 2^1T_2 state at R_e arises from a strongly avoided crossing between these diabatic states. Because the coupling between the diabatic states (red and blue curves) is so strong, we will not find (see next section) a vibrational structure that can be associated with the vibrations in the red or blue potential energy curve but rather vibrations that can be understood from the shape of the adiabatic "2^1T_2" curve (green curve). The "2^1T_2" curve has HOMO → LUMO + 1 character in the regions of the wells because both the $7e \rightarrow 7b_2$ character at positive Q_θ values and the $1a_2 \rightarrow 8e$ character at negative Q_θ values are of the HOMO → LUMO + 1 type. It is important to note that at and in the neighborhood of R_e, the character of "2^1T_2" happens to be different, being of the HOMO − 1 → LUMO type. At that point, there is much mixing, the $1a_2 \rightarrow 8e$ and $7e \rightarrow 7b_2$ contributions are both only 15%, and there is considerable (51%) $6e \rightarrow 2b_1$ character that occurs at larger positive and negative Q_θ values predominantly in the "3^1T_1" curve plus some (17%) $6e \rightarrow 8a_1$ character that is a total of 68% HOMO − 1→ LUMO character. Because this character at R_e is rather atypical for the whole "2^1T_2" curve, we do not feel that it is justified to classify the second band in the spectrum, which represents primarily vibronic structure associated with the "2^1T_2" state, as having HOMO − 1 → LUMO character. The classification, in terms of single orbital excitations, obviously loses its meaning here.

We also recall that the "2^1T_1" curve (orange) corresponds to the $6e \rightarrow 8a_1$ orbital excitation (cf. Table 2, i.e., has HOMO − 1 → LUMO character). Apparently, the HOMO − 1 → LUMO and HOMO → LUMO + 1 characters occur throughout in the same excitation-energy region.

5. Vibronically Coupled Spectra

5.1. Influence of Different Vibrations. We used our model potential energy surfaces to simulate the vibronically coupled absorption spectrum of permanganate. The crucial point in such a simulation is the selection of the quanta distribution for the normal modes.[23] The experimental spectrum is shown at the top of Figure 10 for comparison.

We first simulated a spectrum in which only the totally symmetric mode was populated because totally symmetric modes usually, and particularly in this case,[1,11] dominate the vibrational progression. The corresponding spectrum is shown at the bottom of Figure 7. Clear vibrational progressions of approximately 900−950 cm^{-1} can be observed for all excited states, which reflects the fact that all four model potential energy surfaces exhibit a similar shape and are displaced with respect to the ground-state curve along this normal coordinate (see the upper panel of Figure 5). The dominant experimental vibrational spacings for the first and third electronic transition are about 750 and 770 cm^{-1}, respectively. This is in reasonable agreement with our results in view of the approximations in the model applied here: We use model potential energy curves that are

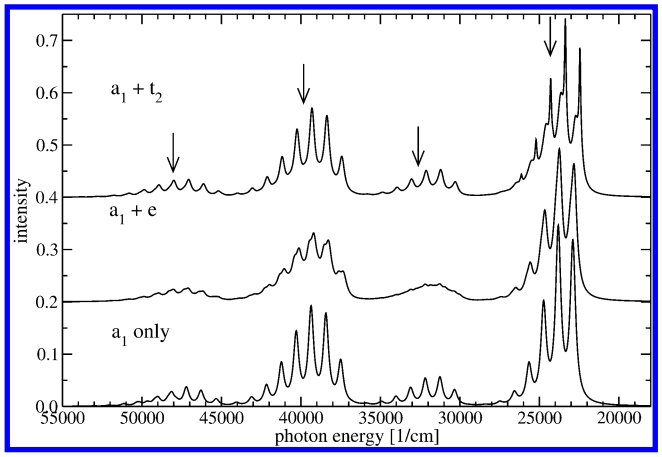

Figure 7. Simulated spectra of MnO_4^- using SAOP/TZ2P. Shown are three simulations in which only the a_1 mode (bottom), modes in irreducible representations a_1 and e (middle), and modes in irreducible representations a_1 and t_2 (top) are populated. The positions of the vertical excitations are marked by arrows. Individual vibronic peaks are represented by Lorentzian curves with a half-width of 0.05 eV (403 cm^{-1}). For better comparability with the experiment, we used a half-width of 0.0125 eV (101 cm^{-1}) in the spectra with the population of the t_2 modes only for the peaks of the a_1 progression in the first band.

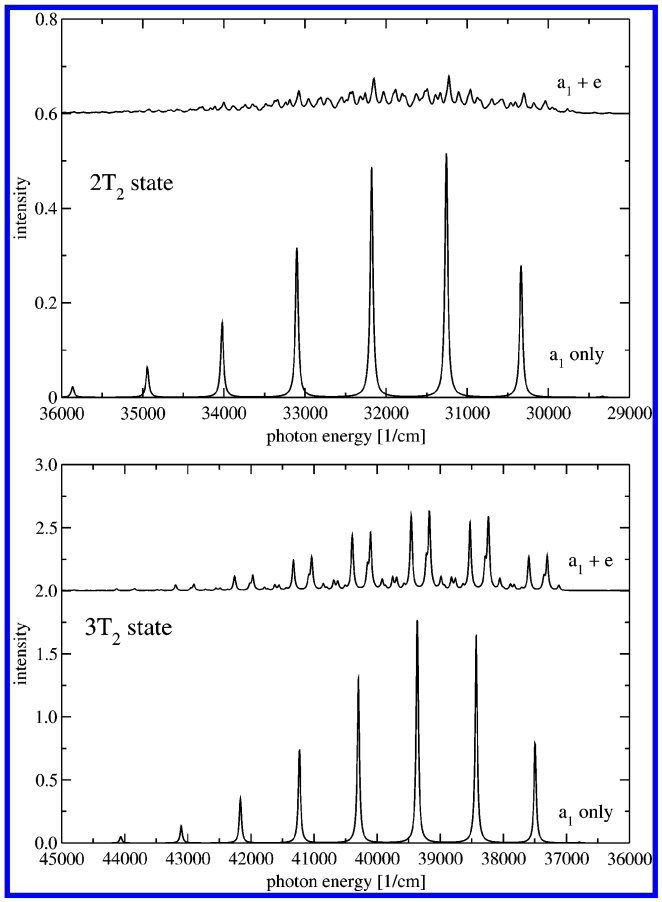

Figure 8. Detailed comparison of the simulated spectra of MnO_4^- using SAOP/TZ2P. Top: simulation of the 2^1T_2 system; bottom: simulation of the 3^1T_2 system. In both cases, simulations are shown in which (i) only a_1 or (ii) a_1 and e modes are populated. Individual vibronic peaks are represented by Lorentzian curves with a half-width of 0.005 eV (40 cm^{-1}).

determined by the second derivatives at the *ground-state* equilibrium position and do not contain anharmonic corrections (i.e., the *diabatic* model curves are quadratic functions). Nevertheless, deviations of the *adiabatic* model curves from the parabolic shape could arise from couplings between different states, which are small in this case.

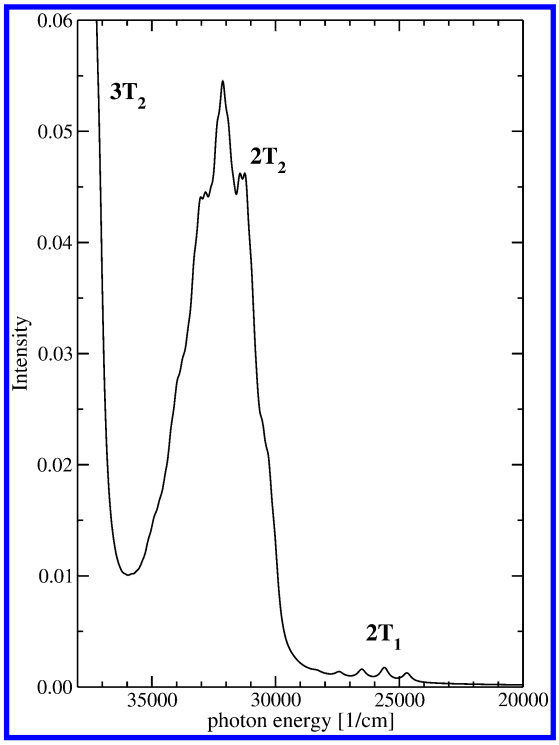

Figure 9. Simulated spectrum of the 2^1T_2 and 2^1T_1 states of MnO_4^- using SAOP/TZ2P. Note that the 3^1T_2 state is also included in the simulation and that the a_1 and e modes are populated. In this simulation, dipole moment derivatives have been taken into account, and the 2^1T_1 state is shifted by −0.6 eV (−4839 cm^{-1}) to separate it from the 2^1T_2 band.

In comparison to the experimental spectrum in ref 1 (see Figure 10), we observe that the calculated vibrational pattern of the lowest excited state is similar, although the intensity of the vibronic transition decreases a bit too quickly for the higher vibrational levels, which is mainly due to the fact that the vibrational frequency is too high. The linear term in the Taylor expansion of the excited-state PES determines the displacement of the excited-state minimum with respect to the ground-state equilibrium structure and therefore the number of vibrational levels accessible from the ground state.

For the second and third excited states, we find qualitative agreement of our simulation and the experiment, although in the experiment the situation is more complicated because of the fact that both bands have a considerable overlap. This is not reproduced in our simulation because of the errors in the vertical excitation energies. In ref 1, the authors come to the conclusion that the high-energy part of the second-band system (between ∼28 000 and 30 000 cm^{-1}) is superimposed on the vibrational progression of the third transition, which should therefore be responsible for the weak vibrational structure in that region, whereas only the first few vibronic transitions in the low-energy part of this band are clearly assigned to the second electronic transition. If only the totally symmetric mode is taken into account, then we see that the second electronic system shows seven peaks in the simulation. Given the difficulty of establishing the vertical transition energies in the experiment, we should leave the possibility open that the vibronic structure in the high-energy region of the second band could also arise from the second electronic transition itself instead of being due to a superposition with the third band. The fourth transition has a rather low intensity in our simulation, whereas the experimental intensity is much higher. In view of the qualitative

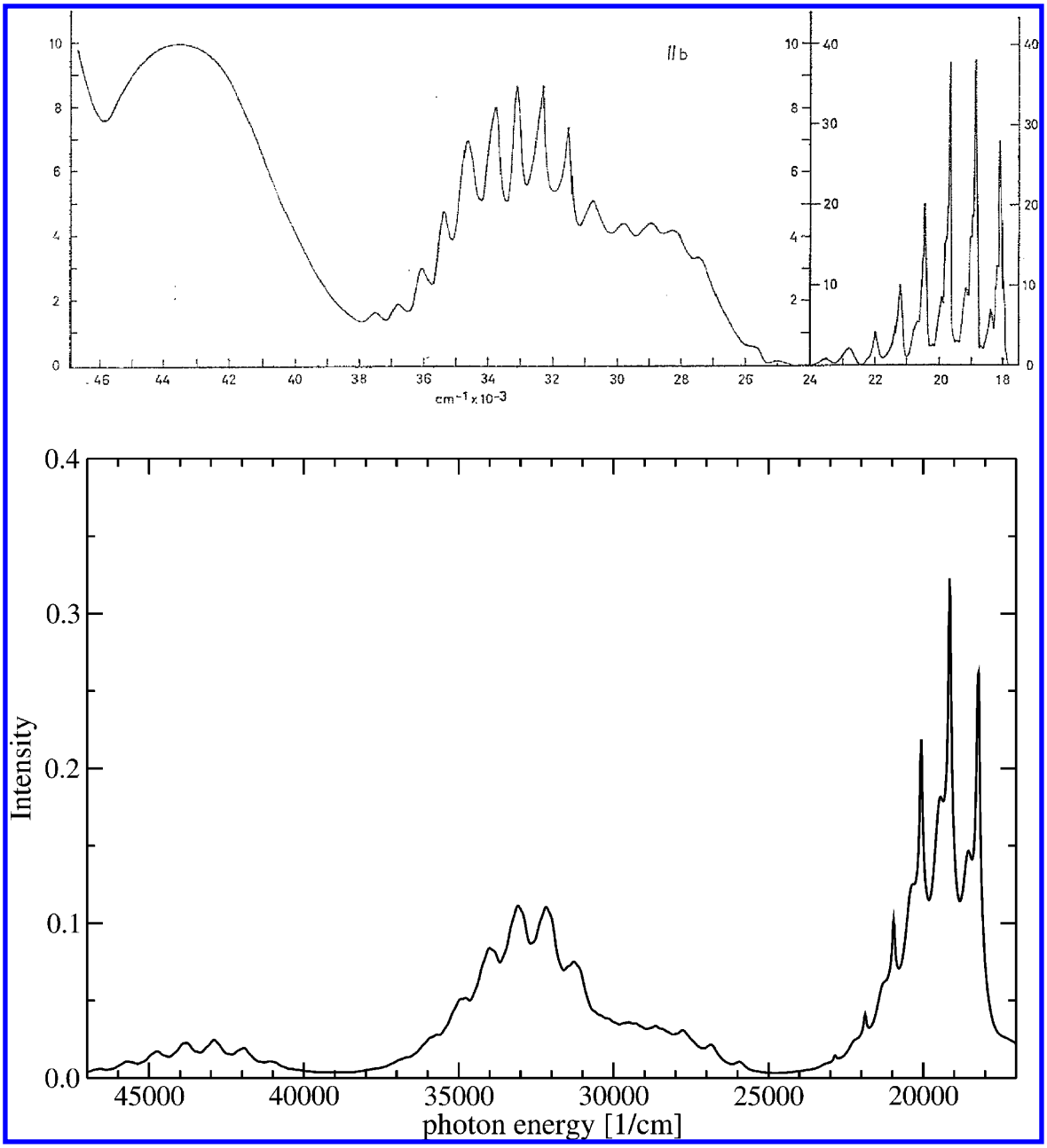

Figure 10. (Top) Experimental absorption spectrum of $KMnO_4$, adapted with permission from ref 1 (copyright by Springer-Verlag, Berlin, 1967). (Bottom) Simulated spectrum; all modes are populated, and vertical excitation energies are shifted (see text).

agreement in the intensities for the other states, we would not expect that the calculated intensity for this state is completely wrong, although it cannot be completely excluded. Another explanation, which is not unlikely considering the problems with the vertical excitation energies, is that the fourth experimental band corresponds to an even higher-lying state, which is missing in our calculation.

If we consider (in addition to the a_1 mode) the effect of the 2-fold-degenerate e modes (Figure 7, middle panel) , which lead to the Jahn−Teller distortions in, for example, the 2^1T_2 state noted above, then we can see that the peculiar blurred vibrational structure of the second band, which is such a striking feature of the experimental spectrum, is now reproduced in the calculations. The third band, however, still exhibits a clear vibrational progression, although all of the peaks appear to be double (show a shoulder), which is due to an excitation of the 2-fold-degenerate e mode in addition to the a_1 stretching mode. A detailed comparison of the vibronic eigenvalue spectrum for the second and third bands is shown in Figure 8, in which a much smaller line width has been used (40 cm^{-1}) to distinguish the different vibronic transitions. It can be seen that the doubling (shoulder) of the a_1 peaks in the 3^1T_2 band arises from the large intensities of two vibrational levels that differ by one quantum in one of the 2-fold-degenerate modes (in addition to the excitation of the a_1 mode) and that very weak peaks for levels with additional quanta in the e modes are also present. That means that each peak of the a_1 progression basically splits into two peaks of comparable intensity, which, in the experimental spectrum, are not resolved but appear as an apparent a_1 progression with broadened peaks.

In the second band system, the peaks from the a_1 progression split into many peaks of comparable intensity: for every peak of the a_1 progression, we now find about seven additional peaks with only slightly lower intensity. This is caused by the shape of the excited-state PES of the "2^1T_2" state, with its negative curvature at $Q_\theta = 0$ and the two minima at positive and negative

displacement along the e modes. As a result, the a_1 progression is barely visible in the second band system if the 2-fold-degenerate modes are taken into account.

Inclusion of the t_2 modes in addition to the a_1 mode introduces significant additional vibrational structure only for the first band. For every peak of the a_1 progression, we find an additional peak with an offset of 335 cm^{-1}, which corresponds to a $|0\rangle \rightarrow |1\rangle$ transition for the t_2 modes. In the experimental spectrum,[1] a similar vibrational structure with an offset of 278 cm^{-1} is found for the a_1 progression, although the peak heights are lower for these vibronic transitions. In our calculation, these peaks become as intense as those of the a_1 progression. This apparent discrepancy might be attributed to the different peak widths in the experimental spectrum, as can be inferred from the upper spectrum in Figure 7 in which the t_2 modes are populated. There we took into account that the experimental peaks of the a_1 progression for the first system are very narrow and used a peak width of 0.0125 eV, whereas all other peaks were modeled with a width of 0.05 eV. The *relative* intensities of the additional peaks follow the same intensity distribution as the corresponding experimental ones.

At this point, we may conclude that the vibronic-structure calculations reproduce the basic features of the experimental spectrum, notably the fact that the vibrational structure in the first and third bands is much better resolved and much more regular than that of the very broad and structureless second band.[1] This supports the assignment of the experimental bands to the excitations with the electronic structure, as given in the DFT-SAOP excitation energy calculations; see the previous section.

5.2. Full Spectrum Simulation Including $^1T_1$ States. Until now, we have taken the (couplings between the) 12 states that arise from the $1-4^1T_2$ multiplets into account. In addition, there are the (at R_e forbidden) $^1T_1$ states; see Figure 5. We have repeated the spectra simulations with inclusion of 2 of the $^1T_1$, the 2^1T_1, and either the 3^1T_1 or the 4^1T_1 states, bringing the total of coupled states to 18. There are, however, hardly any differences for the simulations in which the a_1 mode or the a_1 and e modes are populated. For the third simulation, in which the a_1 and t_2 modes are populated, we have observed that the second band system now shows a less distinct a_1 progression than in the case of inclusion of only $^1T_2$ states; see the upper panel of Figure 7. But because this second band is blurred by the e modes anyway, this does not constitute a noticeable change in the total simulation. We conclude that there are no differences in the total simulation of the allowed transitions with inclusion of the $^1T_1$ states, so their influence on the spectra is small.

By also using a Taylor series expansion of the transition dipole moment analogously to the Herzberg−Teller approach, we can study the question of whether the very low intensity peaks on the low-energy side of the experimental second band (see the upper panel of Figure 10) might be attributed to 2^1T_1 peaks, which acquire intensity due to nonzero transition dipole moments for displaced structures. Although these transition dipole moment derivatives might not be very accurate, we can at least get qualitative information. A simulation with the 2^1T_1 state and transition dipole moments included, in which only the a_1 and e modes are populated, does not lead to observable peaks just below the vibronic structure belonging to the "2^1T_2" state (second band). But again, this might be attributed to the wrong vertical excitation energies because an analysis of the Lanczos eigenvectors shows that some of the peaks in the second band system are due to the 2^1T_1 state, which are too weak in intensity to be recognized in the broad background. To separate the contributions of these two states, we performed a simulation in which the 2^1T_1 state was shifted by −0.6 eV (−4839 cm^{-1}) and only this state, the 2^1T_2, and the 3^1T_2 state were included. The resulting spectrum is shown in Figure 9. The 2^1T_1 state can be seen as a band of very low intensity compared to that of the "allowed" transitions to the 2^1T_2 and 3^1T_2 states but with a clear vibrational progression of about 900 cm^{-1}. Although this is not conclusive evidence, it shows that the two peaks at ca. 25 000 and 25 700 cm^{-1} in the experimental spectrum might indeed originate from the 2^1T_1 state.

TABLE 3: Calculated (SAOP/TZ2P) Excitation Energies (E_{calcd}), Empirical Shifts (ΔE_{emp}), and Best Estimates of the Vertical Excitation Energies (E_{est} in eV) for the Excited States of Irreducible Representation $^1T_2$ of the Permanganate Ion from the Combination of Experimental and Theoretical Data[a]

no.	transition	exptl	E_{calcd}	ΔE_{emp}	E_{est}
1	$1t_1 \rightarrow 2e$	2.3	3.01	−0.54	2.5
2	$6t_2 \rightarrow 2e$	3.5	4.04	−0.44	3.6
3	$1t_1 \rightarrow 7t_2$	4.0	4.93	−0.79	4.1
4	$6t_2 \rightarrow 7t_2$	5.5	5.95	−0.52	5.4

[a] The experimental values shown are the positions of the band maxima of the spectrum reported in ref 1.

The full simulated spectrum (the bottom of Figure 10) combines all of the features described above (24 coupled states and a_1, e, and t_2 modes). Besides the $^1T_2$ states, the four lowest $^1T_1$ excited states have also been included in this simulation. In this spectrum, we corrected the vertical excitation energies by empirical shifts, which are given in Table 3, to obtain a better agreement of the band origins with experiment. Also, the $^1T_1$ states are uniformly shifted in this simulation by −0.5 eV to preserve the correct order of the excited states. It should be noted that this shifting is, from a theoretical point of view, a bit problematic because lower-energy gaps between the excited states in turn often cause larger couplings between the different excited states. This would mean that the interstate coupling constants, which cause such couplings in our simulation, should also be adjusted accordingly. However, there is no direct way to estimate these changes in the coupling constants because we cannot model the effect of smaller energy gaps in the electronic structure calculations. Therefore, no empirical corrections to these coupling constants will be applied. Our empirical shifts of the calculated band origins, to obtain optimal agreement with the experiment, provide "best estimates" of the vertical excitation energies, which are also shown in Table 3.

Except for the wrong total intensity for the fourth band and the slightly too high vibrational spacing for the a_1 progression, we obtain good general agreement with the experimental spectrum. Details of the vibrational quanta distribution for the four simulated spectra shown in Figures 7 and 10 are given in Table 4. Note that *ground-state* vibrational basis functions are employed, and extensive tests have been performed to ensure the convergence of the spectroscopic features with respect to the number of quanta.

6. Discussion and Conclusions

In this study, we have shown that the TDDFT/SAOP method for the calculation of the excitation energies and excited-state potential energy curves, combined with a vibronic coupling method that uses the TDDFT transition densities in the diabatization method, is a powerful tool for the simulation of the vibronic structure of absorption spectra. In view of its efficiency, it can be applied to large systems, such as transition-metal complexes. For the permanganate anion, it leads to good

TABLE 4: Distribution of the Vibrational Basis Functions (Number of Quanta + 1) to the Normal Modes in the Four Simulations of the Absorption Spectrum of Permanganate Shown in Figures 7 and 10[a]

vibration	ν_{a_1}	ν_e	ν_{1t_2}	ν_{2t_2}
ground state	878	351	401	940
exptl	(845)	(350)	(400)	(930)
a_1 only	100	1	1	1
$a_1 + e$	20	20	1	1
$a_1 + t_2$	20	1	5	2
full simulation	20	12	4	2

[a] Also shown are the ground-state frequencies (BPW91/TZ2P; in units of cm^{-1}) of these vibrations (experimental values[42,43] are given in parentheses). In the case of the degenerate modes, the given number of quanta was used for each of the modes of the degenerate set.

agreement with the experimental spectrum and helps us to understand the nature of the transitions. The quality of the simulation suggests that the long-standing assignment problem for the second and third allowed electronic transitions is resolved. Our simulation reproduces the salient features of the experimental spectrum. That is, the second band system is very broad and almost without vibrational structure, whereas the third band shows a clear progression from the totally symmetric stretching mode. The broadening in the second band system is due to the double-well nature of the PES along the modes of e symmetry, leading to many vibrational states with nonzero transition dipole moments from the ground state. In the third band system, the excited-state PES has just a single minimum along the e mode, which is only slightly displaced from R_e, and a roughly parabolic shape around the minimum. Including the e mode vibronic states leads to shoulders on the peaks (overlapping double peaks) of the a_1 progression, which remains the dominant feature of the vibrational structure of this band. The simulated spectra also reproduce a clear vibrational structure in the first band system because of the a_1 progression, augmented with additional peaks that can be attributed to higher vibrational quanta in the t_2 modes. Also, the intensity distribution for the first three band systems is in qualitative agreement with experiment. The highest peaks occur for the first system, and the peaks in the third system also show considerable intensity, whereas the second band is less intense.

The vibronic structure serves as a kind of fingerprint for the underlying PESs and the nonadiabatic coupling between states. We conclude from the agreement between theory and experiment that our calculations probably yield a correct interpretation of the electronic structure. One should be aware, of course, that agreement between the calculated and experimental vibronic structure is a necessary but not sufficient condition for the theoretical assignment to be correct. Regarding the electronic nature of the excitations, we have noted that it is not meaningful to assign the second and third bands to single orbital transitions. There is strong configuration mixing, which changes along, for example, the e mode. We have identified the Jahn−Teller splitting in the 3d manifold of t_2 symmetry along the e mode as the origin of the double-well structure of the 2^1T_2 PES and, hence, as the origin of the blurring of the vibrational structure in the second band.

In contrast to the good agreement for the vibronic structure, the vertical excitation energies are not very accurate. They are all too high, but they are not uniformly too high (i.e., the spacing is also incorrect). The band origins differ by several thousand cm^{-1}, and the second and third bands do not overlap in our calculation. However, environmental effects have been completely neglected in our study, whereas the experimental spectrum was obtained for $KMnO_4$ in a $KClO_4$ crystal. Furthermore, the simulated spectra show that the positions of the band maxima, which are used in the experiment to estimate the vertical transition energies, are only a rough measure for the vertical excitation energies. The latter can be more than 1000 cm^{-1} higher than the band maxima. This effect would reduce the errors in the vertical excitation energies a bit: The calculated band maxima are at approximately 2.90 (1^1T_2), 3.85 (2^1T_2), 4.85 (3^1T_2), and 5.85 eV (4^1T_2). This is closer to the experimental band maxima than the calculated vertical transition energies (cf. Table 3), but deviations between the experimental and calculated band maxima of 0.3 to 0.8 eV would still remain. Furthermore, the incorrect spacing also remains (e.g., these effects do not lead to an overlap of the second and third transitions), which is observed in the experiment. By applying empirical corrections to the calculated vertical excitation energies, we were able to achieve very good agreement of the general appearance of the absorption spectrum of MnO_4^- compared to that of the experiment for the first three bands. The full vibronic structure of an absorption band gives a much more characteristic signature of an electronic absorption and provides a much richer target for theoretical comparison than the experimental vertical excitation energy alone (necessarily a rough estimate, e.g., the band maximum). For the high-lying fourth band system, we do not obtain the high experimental intensity. Also, other experimental studies[40,41] do not offer possible explanations for this experimental feature. Whether even higher-lying states are playing a role here needs to be investigated.

To summarize, our study shows that the vibronic structure simulation of transition-metal absorption spectra within the short-time approximation yields very satisfactory results, so the vibronic structure can be used as a fingerprint for the assignment of electronic bands because even details (e.g., the effects originating from the Jahn−Teller active modes) can be modeled correctly. The method does not rely on excited-state structure optimizations and is capable of describing nonadiabatic couplings between (near-)degenerate excited states. Therefore, it is particularly well suited for transition-metal complexes with close-lying PESs or complicated excited-state topologies. It can be applied in a straightforward manner and is generally applicable, which provides confidence for the application of this method to larger molecules.

Acknowledgment. This work was partly supported by a discovery grant from the Natural Sciences and Engineering Research Counsel of Canada (NSERC). J.N. gratefully acknowledges funding by a Forschungsstipendium of the Deutsche Forschungsgemeinschaft (DFG).

References and Notes

(1) Holt, S. L.; Ballhausen, C. J. *Theor. Chim. Acta* **1967**, *7*, 313−320.
(2) Ballhausen, C. J.; Gray, H. B. Electronic Structures of Metal Complexes. In *Coordination Chemistry*; Martell, A. E., Ed.; Van Nostrand Reinhold: New York, 1971; Vol. 1.
(3) Nakai, H.; Ohmori, Y.; Nakatsuji, H. *J. Chem. Phys.* **1991**, *95*, 8287−8291.
(4) Wolfsberg, M.; Helmholtz, L. *J. Chem. Phys.* **1952**, *20*, 837.
(5) Ballhausen, C. J.; Liehr, A. D. *J. Mol. Spectrosc.* **1958**, *2*, 343.
(6) Viste, A.; Gray, H. B. *Inorg. Chem.* **1964**, *3*, 1113.
(7) Johnson, K. H.; Smith, F. C., Jr. *Chem. Phys. Lett.* **1971**, *10*, 219−223.
(8) Baerends, E. J.; Ellis, D. E.; Ros, P. *Chem. Phys.* **1973**, *2*, 41−51.
(9) Ziegler, T.; Rauk, A.; Baerends, E. J. *Chem. Phys.* **1976**, *16*, 209−217.
(10) Dickson, R. M.; Ziegler, T. *Int. J. Quantum Chem.* **1996**, *58*, 681−687.
(11) Stückl, A. C.; Daul, C. A.; Güdel, H. U. *J. Chem. Phys.* **1997**, *107*, 4606−4617.

(12) Atanasov, M.; Brunold, T. C.; Güdel, H. U.; Daul, C. *Inorg. Chem.* **1998**, *37*, 4589−4602.
(13) Stückl, A. C.; Daul, C. A.; Güdel, H. U. *Int. J. Quantum Chem.* **1997**, *61*, 579−588.
(14) van Gisbergen, S. J. A.; Groeneveld, J. A.; Rosa, A.; Snijders, J. G.; Baerends, E. J. *J. Phys. Chem. A* **1999**, *103*, 6835−6844.
(15) Boulet, P.; Chermette, H.; Daul, C.; Gilardoni, F.; Rogemond, F.; Weber, J.; Zuber, G. *J. Phys. Chem. A* **2001**, *105*, 885−894.
(16) Hillier, I. H.; Saunders, V. R. *Chem. Phys. Lett.* **1971**, *9*, 219.
(17) Johansen, H. *Chem. Phys. Lett.* **1972**, *17*, 569.
(18) Johansen, H.; Rettrup, S. *Chem. Phys.* **1983**, *74*, 77−81.
(19) Nooijen, M. *J. Chem. Phys.* **1999**, *111*, 10815−10826.
(20) Nooijen, M.; Lotrich, V. *J. Chem. Phys.* **2000**, *113*, 494−507.
(21) Dierksen, M.; Grimme, S. *J. Chem. Phys.* **2004**, *120*, 3544−3554.
(22) Dierksen, M.; Grimme, S. *J. Phys. Chem. A* **2004**, *108*, 10225−10237.
(23) Nooijen, M. *Int. J. Quantum Chem.* **2003**, *95*, 768−783.
(24) Heller, E. J. *Acc. Chem. Res.* **1981**, *14*, 368−375.
(25) Heller, E. J.; Sundberg, R. L.; Tannor, D. *J. Phys. Chem.* **1982**, *86*, 1822−1833.
(26) Myers, A. B. *Chem. Rev.* **1996**, *96*, 911−926.
(27) Myers, A. B. *Acc. Chem. Res.* **1997**, *30*, 519−527.
(28) Köppel, H.; Domcke, W.; Cederbaum, L. S. *Adv. Chem. Phys* **1984**, *57*, 59.
(29) Neugebauer, J.; Hess, B. A. *J. Chem. Phys.* **2004**, *120*, 11564−11577.
(30) Schipper, P. R. T.; Gritsenko, O. V.; van Gisbergen, S. J. A.; Baerends, E. J. *J. Chem. Phys.* **2000**, *112*, 1344−1352.
(31) Gritsenko, O. V.; Schipper, P. R. T.; Baerends, E. J. *Chem. Phys. Lett.* **1999**, *302*, 199−207.
(32) Gritsenko, O. V.; Schipper, P. R. T.; Baerends, E. J. *Int. J. Quantum Chem.* **2000**, *76*, 407−419.
(33) *ADF*; Density Functional Theory (DFT) software for chemists. http://www.scm.com.
(34) te Velde, G.; Bickelhaupt, F. M.; Baerends, E. J.; van Gisbergen, S. J. A.; Guerra, C. F.; Snijders, J. G.; Ziegler, T. *J. Comput. Chem.* **2001**, *22*, 931−967.
(35) Neugebauer, J.; Baerends, E. J.; Nooijen, M. *J. Chem. Phys.* **2004**, *121*, 6155−6166.
(36) Nooijen, M.; Hazra, A. *VIBRON;* a program for vibronic coupling and Franck−Condon calculations, with contributions from John Stanton and Kurt Sattelmeyer; University of Waterloo, 2003.
(37) Seth, M.; Ziegler, T.; Banerjee, A.; Autschbach, J.; van Gisbergen, S. J. A.; Baerends, E. J. *J. Chem. Phys.* **2004**, *120*, 10942−10954.
(38) Bersuker, I. B. *The Jahn−Teller Effect and Vibronic Interactions in Modern Chemistry*; Plenum Press: New York, 1984.
(39) Bersuker, I. B. *Coord. Chem. Rev.* **1975**, *14*, 357−412.
(40) Johnson, L. W.; McGlynn, S. P. *Chem. Phys. Lett.* **1971**, *10*, 595−599.
(41) Johnson, L. W.; McGlynn, S. P. *J. Chem. Phys.* **1971**, *55*, 2985−2989.
(42) Müller, A.; Baran, E. J.; Carter, R. O. *Struct. Bonding (Berlin)* **1976**, *26*, 81−139.
(43) Müller, A.; Krebs, B. *Z. Naturforsch., A: Astrophys., Phys. Phys. Chem.* **1966**, *21b*, 3.